JOURNAL OF AIRCRAFT
Vol. 45, No. 5, September–October 2008

Wind-Tunnel Studies of Damaged-Wing-Induced Limit Cycle Oscillations

Hyeonsu Park,[*] Ronald Stearman,[†] Taekhyun Kim,[*] and Edward J. Powers[‡]
The University of Texas at Austin, Austin, Texas 78712

DOI: 10.2514/1.31451

The influence of damage on the performance of the lifting surface of an aircraft has been an area of interest to the military for over half a century. Some of the earlier studies of this subject focused on the impact that structural damage resulting in the loss of lifting surface structural strength, stiffness, and mass might have on imparting catastrophic aeroelastic failures to the lifting surface. Discouraging mixed results arose over the next 30 years in these investigations that employed only structural damage models. As time passed, it was finally noticed that if the often neglected, usually second-order, drag term was now included (as aerodynamic damage often creates a high, unsteady, localized drag rise) in the earlier aeroelastic damaged-wing analyses, more encouraging results were obtained. That is, the realistic asymmetric damaged lifting surfaces flutter and divergence analysis did show lowered, and not raised, flutter and divergence speeds over that of the undamaged lifting surface. This occurred both in the presence of or in the absence of structural damage as in the case of icing or external wing stores. In essence, it was determined at this time that the resulting high and unsteady drag rise caused by the damage could do more than just cause an energy deficiency in the aircraft mission. It could, in fact, cause shorter term catastrophic or stiffness failure events in terms of reduced flutter and divergence speeds as well as give rise to limit cycle oscillations embedded within what was shown to be that part of the damaged-aircraft flight envelope free from classic flutter and divergence. The present experimental wind-tunnel study was carried out to confirm these past theoretical findings by employing a one-twelfth-scale F-111 aeroelastic model and (third-order) higher-order statistical signal processing to identify the frequency ordering that occurs in these additional damaged-induced limit cycle oscillations. These limit cycle oscillations were also found to exhibit the classic lock-in/lock-out phenomenon that occurs in the well-known F/A-16 and F/A-18 wing store induced limit cycle oscillations.

Nomenclature

C = modal damping matrix
$F(t)$ = classical forcing function
$H_C(i, j, l)$ = cubic frequency-domain Volterra transfer function
$H_L(k)$ = linear frequency-domain Volterra transfer function
$H_Q(i, j)$ = quadratic frequency-domain Volterra transfer function
$K(t)$ = modal stiffness matrix which may vary with time
M = modal mass matrix
$P_C(k)$ = output of the cubic component of the Volterra model
$P_L(k)$ = output of the linear component of the Volterra model
$P_Q(k)$ = output of the quadratic component of the Volterra model
$P_Y(k)$ = true observed response power spectrum
$P_{\hat{Y}}(k)$ = estimated response power spectrum of the Volterra model
q = set of generalized coordinates
S_{XX} = power Spectrum of $X(l)$
S_{XXX} = bispectrum of $X(l)$
S_{XXXX} = trispectrum of $X(l)$
$X(l)$ = calculated value of the discrete Fourier transform of $x(n)$
$x(n)$ = nth sampled value of a digital time series
$Y(l)$ = calculated value of the discrete Fourier transform of $y(n)$
$y(n)$ = nth sampled value of a digital time series
$\gamma_C^2(k)$ = cubic coherence spectrum
$\gamma_L^2(k)$ = linear coherence spectrum
$\gamma_Q^2(k)$ = quadratic coherence spectrum
$\gamma_{\mathrm{total}}^2(k)$ = total coherence spectrum
Ω_{f_i} = fluid modal frequencies
$\omega_i, \omega_j, \omega_n$ = normal mode structural frequencies

I. Introduction

OUR interest in the damaged-wing problem started in the late 1970s at the prompting of the Air Force Office of Scientific Research (AFOSR) and the Eglin Armament Lab, who were concerned with warhead-induced lifting surface damage on the aircraft flight characteristics. This interest has since expanded to the damage of lifting surfaces because of both icing damage and bird strike damage. The specific areas of primary concern relate to the impact of the lifting surface damage to the aircraft aeroelastic integrity and to its stability and control characteristics. Many aircraft have encountered lifting surface battle damage while engaged in combat[§] [¶]. They have encountered leading-edge wing and/or tail damage, respectively, as they entered the combat zone. One high drag rise feature occurs when the damage exposes the blunt face of the lifting surface spars to the oncoming flow, which is then diverted both upward and downward as it hits these exposed flat spars. Flow through this damaged hole, in turn, creates a jet spoiler effect and significant unsteady lift, moment, and drag forces resulting from a separated unsteady wake flow localized at this damage site. Our earlier Air Force wind-tunnel studies on damaged

---

Presented as Paper 1799 at the 48th AIAA/ASME/ASCE/AHS/ASC Structures, Structural Dynamics, and Materials Conference, Honolulu, HI, 23–26 April 2007; received 5 April 2007; revision received 21 December 2007; accepted for publication 12 January 2008. Copyright © 2008 by the American Institute of Aeronautics and Astronautics, Inc. All rights reserved. Copies of this paper may be made for personal or internal use, on condition that the copier pay the $10.00 per-copy fee to the Copyright Clearance Center, Inc., 222 Rosewood Drive, Danvers, MA 01923; include the code 0021-8669/08 $10.00 in correspondence with the CCC.

[*] Graduate Student, Department of Electrical and Computer Engineering.

[†] Professor, Department of Aerospace Engineering and Engineering Mechanics. Associate Fellow AIAA.

[‡] Professor, Department of Electrical and Computer Engineering.

[§] Data available online at http://www.aircraftresourcecenter.com/Stories1/001-100/0016_A-10-battle-damage/story0016.htm [retrieved 28 March 2007].

[¶] Data available online at http://www.takhli.org/bob/MemoryJoggersFromBenShuppert3.htm [retrieved 28 March 2007].

lifting surfaces illustrated that the perturbation air loads due to this localized damage remains confined to this local damage site for the lower angles of attack of the lifting surface [1,2]. At the higher angles of attack of approximately 6 deg through stall, however, the effect of the localized damage propagates significantly over the lifting surface and its controls. Past experience indicates that such a sudden significant flow separation over a major portion of the lifting surface could possibly cause a control force reversal, giving rise to a flight upset of the aircraft. The present experimental study will also illustrate that this resulting unsteady wake, generating high unsteady aerodynamic forces due to the damage, can also give rise to possible limit cycle oscillations of these damaged lifting surfaces.

One significant feature of ice formations on wing leading edges characterizes another form of lifting surface damage**. It involves the extensive growth of the ice normal to the wing near its leading edge. This is sometimes referred to as an "ice horn" [3]. It can lead to a significant separation bubble right behind this ice horn at the wing leading edge. Icing wind-tunnel studies on wings have shown that this bubble will also become dynamically unstable at about 6 deg angle of attack [3]. The implication of this unstable bubble dynamic action at the higher angles of attack is that the local flow in the bubble area does not remain attached to the wing in a time-averaged sense [3]. Recent wind-tunnel studies with aeroelastic wing models with icing simulation indicate that such bubble dynamics can lead to a limit cycle oscillation of the wing, or a control snatch with a possible aircraft stability and control upset [3]. This gives rise to yet another nonlinear limit cycle oscillation (LCO) mechanism in addition to the vortex jet spoiler wake phenomenon. In summary, a significant separation bubble is generally found right behind this icing horn or any similar shaped mechanical damage, which can lead to critical aircraft LCOs and/or stability and control upsets.

Yet another damage form is that caused by a bird strike of the lifting surface in flight. Most incidents occur during takeoff or landing at airports, although some have occurred over landfills at 1000–2000 ft altitude. In general, however, most bird strikes occur below 500 ft [4]. About 13 ducks and/or geese have been struck, however, above 20,000 ft, whereas one strike has been reported above 37,000 ft [4]. Bird strikes can do significant damage to a lifting surface. The bird strike problem is considered to be a major cost to the airlines globally. About $1.2 billion annually is estimated as the financial impact on the global airline business [5].

Although three distinctly different lifting surface damage sources are identified here, they all lead to one fundamental unsteady fluid flow problem, which is basically the separated flow phenomenon. Generally, this occurs in the form of a vortex wake and/or a separation bubble or bubbles. The separation bubbles can become dynamically unstable and may burst under certain flight conditions, possibly leading to catastrophic aircraft aeroelastic and/or stability and control upset situations [3]. The generated vortex fluid wake frequencies can phase lock with structural mode frequencies producing limit cycle oscillations of the lifting surfaces, also possibly upsetting the aircraft flight path [6].

In this paper, a specific type of lifting surface damage was considered that generates a high drag rise due to the formation of a fluid jet spoiler arising from the flow around and through the damaged lifting surface leading-edge region. It is an anticipated event as the aircraft enters the combat zone. Furthermore, it has been identified as one of the several types of wing battle damage classes that create the highest localized drag rise [7]. A damage of this type gives rise to a periodic or random wake shedding event, which may be considered as a space time limit cycle in the local fluid motion over the wing. It is well known that the periodic or random fluid wake modes can tune in a classical linear resonance manner to structural mode frequencies giving rise to classical resonances in the structure. Other frequency tunings can also occur, which are consistent with nonlinear resonance phenomenon because separated flow, and, hence, nonlinear forcing mechanisms are present on the structural system.

T. von Kármán, L. Dunn, and R. H. Scanlan are research scientists who were historically involved and who are now commonly associated with such vortex wake flow and structural response interactions [8,9]. The aeroelastic failure of the famous Tacoma Narrows Bridge on 7 November 1940, and the resulting work of these researchers and other investigators on this problem, brought to focus the history of this wind-induced structural excitation. It appears to have first been practically employed as early as the Aeolian Harp in King David's time [8]. Associated with this excitation event, is the observation that when the blunt structure experiencing the flow is at rest in the flow field, and the classical wake frequency as determined by the flow Strouhal number for the structural shape coincides or tunes with one of the structural mode frequencies, the fluid forcing frequencies may excite the structure into motion. Once the motion starts, it has been demonstrated, experimentally, that the frequency of oscillation "locks into and is controlled by the structural motion and not its shape or the velocity of the flow" [8]. That is, as the flow velocity and the corresponding Strouhal frequency increases, the oscillations stay locked into the blunt body structural motion frequency. It has been further pointed out by these investigators, however, that after this "lock in" has occurred, the flow velocity continues to increase after a significant mismatch occurs between the locked in lower structural vibration frequency, and the Strouhal number frequency of the flow the structural motion suddenly ceases. At this point, the so-called lock out has occurred. This experimentally observed phenomenon of lock in and lock out is not well understood at the present time, but is considered by all experts to be a highly nonlinear phenomenon. Scanlan et al. pointed out in a recent text on aeroelasticity that the sudden occurrence of this frequency of structural response event is known as lock in [9]. This paper has used higher-order signal processing tools to demonstrate, experimentally, this lock-in/lock-out occurrence for the special type of vortex wake induced damaged-wing LCO studied here.

Section II outlines the categories of various aerodynamic damage and introduces aeroelastic damage models for study. In Sec. III, our experimental wind-tunnel model of an isolated F-111 wing are introduced, and a schematic of the data acquisition system is presented. In Sec. IV, phase 1 damaged-wing wind-tunnel studies previously performed are described, and the motivation of this paper is indicated. In Sec. V, our frequency-domain orthogonal Volterra model analysis is presented. We explain how to determine the parameters of our model using second- and higher-order statistics. In Sec. VI, the experimental configuration employed to acquire the hot wire and accelerometer time series data is explained. In addition, analyses and results of our experimental studies are provided to demonstrate an earlier observed phenomenon of lock in/lock out, which was also encountered in these damaged-wing LCO events. Finally, we conclude our experimental studies in Sec. VII.

II. Aerodynamic Damage Model

The general aerodynamic lifting surface damage geometries of interest in this study are identified in Figs. 1–5. Figure 1 illustrates two aircraft lifting surfaces, the pilot's A-10 right stabilizer and the F-105 right wing, that have encountered battle damage while engaged in combat.[§] It is apparent that the blunt spar faces exposed due to these through hole damages will create a jet spoiler effect due to the airflow blockage by the spars, as previously mentioned. This, in turn, will create a vortex wake flow in the localized region behind the damage zone. This vortex wake will create significant localized periodic unsteady aerodynamic lift, moment, and drag forces to act on the lifting surface behind this localized damage area for certain lifting surface angle of attack conditions. For other flight conditions, which occur at higher angles of attack of the lifting surface, approximately 6 deg through stall, the separated flow effects do not remain localized but propagate over a significant region of the lifting surface flowfield just as we observe in the classic wing stall phenomenon. This may have first been observed in the late 1970s in wind-tunnel studies on the damaged T-38 stabilator in the low-speed

---

[**] Data available online at http://weather.aero/icing/case_wing2.jpg [retrieved 28 March 2007].

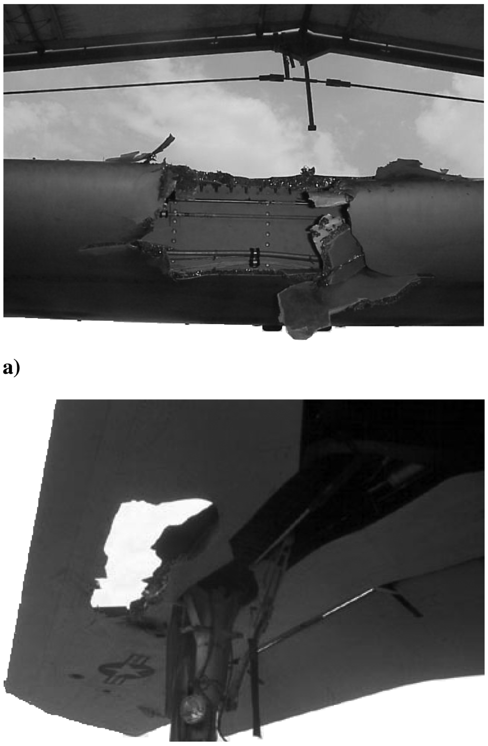

a)

b)

Fig. 1 Examples of lifting surface battle damage: a) pilot's A-10 right stabilizer showing exposure of main spar to flow, and b) pilot's F-105 right wing with a through hole damage exposing internal wing structure to flow.

wind-tunnel shown in Fig. 4b [2]. Figure 5 shows the extent of the through hole geometries investigated in this T-38 left stabilator during this wind-tunnel test. This lack of aerodynamic damage localization at the higher angles of attack was observed in all of these through hole damage cases studied. This was first identified by us as shown in Fig. 6, which illustrates the spanwise lift distribution determined from the integration of the measured chordwise pressure distributions on the one T-38 stabilator wind-tunnel model equipped with pressure taps [1,2].

Another form of lifting surface damage is shown in Fig. 2, which is caused by ice formation on lifting surfaces usually most prominent at their leading edges. An interesting aerodynamic damage spreading condition also occurs in this case starting at approximately 6 deg due to dynamic stability problems in the separation bubble just behind the ice buildups. This mechanism is discussed by Bragg in several related icing studies on lifting surfaces [10]. Figures 3a and 3b illustrate yet another form of lifting surface damage that can be created by a bird strike to a lifting surface. The particular event illustrated here occurred on a general aviation aircraft metal wing that was flying at an altitude of approximately 1900 ft above ground level in the vicinity of what was thought to be a landfill area. The impact damage is compared in Fig. 3b to an FAA-catalogued extreme horned icing form.

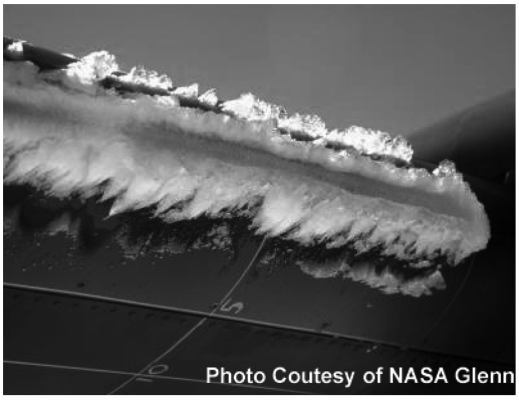

Photo Coutesy of NASA Glenn

Fig. 2 Mixed ice formations on airfoils.[**]

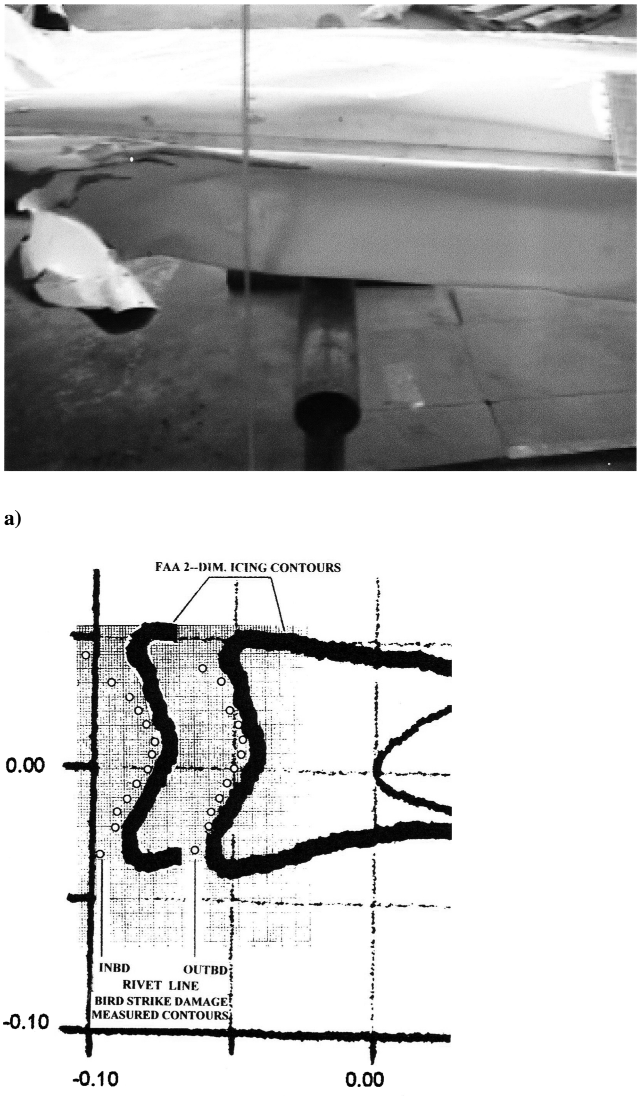

a)

b)

Fig. 3 Bird impact: a) to the left wing leading edge of a general aviation aircraft showing significant leading-edge concave damage, and b) damage compared with FAA horn icing contours.

Figure 4a illustrates the theoretical aerodynamic damage model developed after extensive wind-tunnel studies were conducted at both the subsonic and transonic speeds investigating various classes of warhead damage imposed on different lifting surfaces. The reader is referred to [11] for additional details on this study. Figure 4b illustrates a study conducted on a damaged T-38 full scale stabilator in our 5 by 7 ft low-speed tunnel at the University of Texas Pickle Research Campus. This model contained 15 static pressure orifices each located at ten spanwise stations. A sidewall force balance was also installed. The operating Reynolds number averaged 5.29×10^6 based upon the mean aerodynamic chord. Figure 5 illustrates the through-hole damage sizes tested as well as the model dimensions and aerodynamic characteristics. Two types of spanwise lift distributions are shown in Fig. 6 for the 1% through-hole damage illustrated in Fig. 5 at the two angles of attack conditions. These spanwise lift distributions were obtained by integrating some 150 measured chordwise pressure distributions for various test conditions. The two lift distributions shown in Fig. 6 illustrate the essential features used to develop our localized aerodynamic damage modeling. Essentially, it illustrates the confinement of the perturbation pressure fields when only a localized damage occurs on the lifting surface, as long as the lifting surface angle of attack is

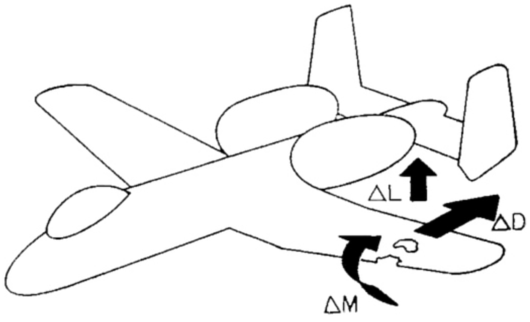

a)

b)

Fig. 4 Development of a localized aeroelastic damage model [11].

small. When, however, the angle of attack is large, 6 deg or more, the perturbation pressures due to the localized damage propagate over the complete span, influencing the entire surface. It should be noted that this is also the angle of attack when the separation bubble due to the icing damage has been observed to go dynamically unstable [10]. In essence, these results were used to justify the aerodynamic damage model, for the low angles of attack found at cruise. Furthermore, the features of the localized jet spoiler damage-induced perturbation air loads were measured on a static aerodynamic lifting surface and the measured shedding vortex-induced air load frequencies were then used in a quasi-static approximation (i.e., on a damaged-wing without motion) by coupling this damaged wake measurement with an unsteady aerodynamic transient lifting surface theory to estimate LCOs and/or flutter events triggered by the damage. We justify this approach based upon the observed lock-in phenomenon. In summary, employing this static localized aerodynamic damage frequency modeling, suggested in Fig. 4a, seems plausible for both cruise conditions and damaged events experiencing lock in. This model would not be acceptable, obviously, if studies concerning high angle stall flutter or if maneuvering dynamics at high angles of attack were of interest when aerodynamic wing damage is present.

III. Experimental Wind-Tunnel Models

Figure 7 illustrates the isolated F-111 aeroelastic wing wind-tunnel model employed in the first phase (phase 1) of the damaged-wing limit cycle testing. The base line model was designed by the former Wright–Patterson Flight Dynamics Lab for the variable swept wing and tail interference wind-tunnel flutter studies. This model design was supplied to us by the Flight Dynamics Lab for the damaged-wing Air Force limit cycle studies. Because the model under study is a stick and pod aeroelastic model design, it does not exhibit the multispar design of the full-scale aircraft and will not exhibit the correct aerodynamic unsteady drag force that will be generated by the full-scale wing exhibiting the exposed wing spar with jet spoiler effect. As the result of this drag force mismatch, an equivalent flat plate drag element is added to the model. Several different flat plate configurations were used. The through-hole effect was obtained by removing the pod covers. The complete through hole wing damage model is illustrated in Fig. 7 as mounted in our open 2 by 3 ft subsonic test section wind tunnel. Figure 8 illustrates the instrumentation employed to carry out the data acquisition and the analog recording of the sensor signals in the wind-tunnel test along with a video camera to record the limit cycle oscillations. The dynamic signal components of the hot wire and accelerometer were employed in the required signal processing. The recording of the test data was accomplished with a Honeywell Model 101 analog recorder. More description regarding this experimental configuration is explained in Sec. VI.

The complete wing-tail flutter model employed in the phase 2 limit cycle studies is shown in Fig. 9 as mounted from the ceiling of our large 5 by 7 ft subsonic wind tunnel. The model description is also presented in Fig. 9. The pressure pod sensor in Fig. 9 serves as the input to our signal processing as opposed to the unsteady hot-wire measurements in our smaller tunnel phase 1 studies illustrated in Fig. 7. The further information related to the phase 2 studies will be available in future work.

IV. Results of Previous Phase 1 Damaged-Wing Wind-Tunnel Studies

Still air vibration studies of the damaged-wing employed in the phase 1 model studies were conducted with this isolated wing model in Fig. 7 mounted in the wind tunnel [11]. Whereas the presence of the air stream will modify these still air vibration modes and frequencies to some extent, these results are very helpful in determining the frequency selection rules that occur when investigating the energy flows between the fluid normal modes generated in the damage wake flow locking in to the structural normal modes at air speed. This fluid wake locking in to the structural normal modes generates the wing limit cycle oscillations. The most dominant fluid normal modes Ω_{f_1} and Ω_{f_2}, that first lock in, in a difference sense, to structural mode first torsional frequency ω_n at the air speed of limit cycle occurrence corresponds to the "mixed mode" of frequency selection options shown in Fig. 10. This corresponds to the difference of the wake unsteady lift, moment frequency Ω_{f_1} (classical forcing), and the unsteady drag frequency Ω_{f_2} (parametric forcing) of approximately 25–27 Hz, coinciding with the first structural mode frequency ω_n at an air speed of approximately 27 Hz. Figure 10 depicts the proposed theoretical aeroelastic modeling equations, including both the aerodynamic and structural dynamic damage models using a transient aerodynamic strip theory along with the frequency selection tuning rules promoting LCO phenomenon [11]. A formal solution of these equations results in a few examples of limit cycle occurrences within regions of the flight envelopes free of flutter and divergence as depicted at points 1, 2, 3, 4, 5, and 6 in Fig. 11.

The phase 1 isolated damage wing wind-tunnel studies supported the theoretical findings derived from the equations shown in Fig. 10. These equations represent the aeroelastic theoretical formulization of the damaged-wing studies that predicted the limit cycle instabilities, in addition to the traditional flutter and divergence instabilities. That is, when the proposed aerodynamic damage modeling was included

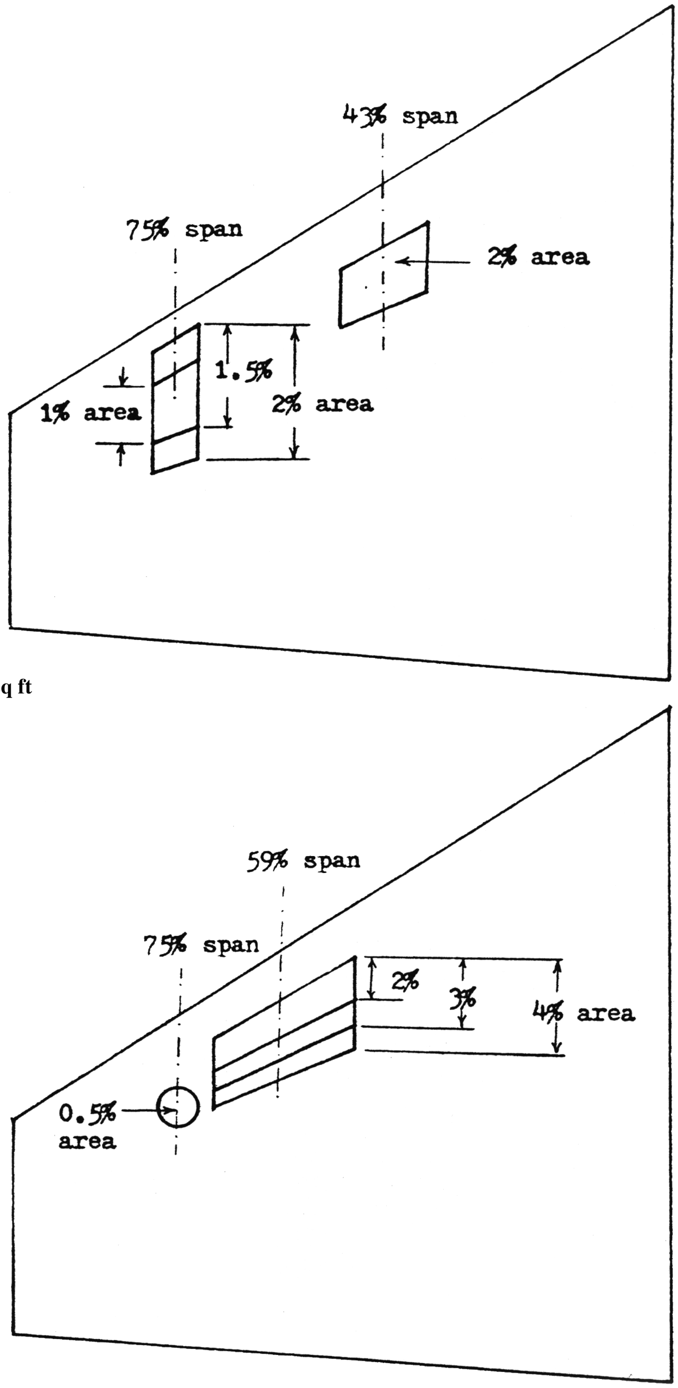

Airfoil Section	**-**	**65A004**
Planform Area	**-**	**1.626 sq m; 17.50 sq ft**
Semispan	**-**	**1.544 m; 60.78 in.**
Root Chord	**-**	**1.589 m; 62.90 in.**
Tip Chord	**-**	**0.508 m; 20.00 in.**
Leading - Edge Sweep	**-**	**32.7 deg**
Trailing - Edge Sweep	**-**	**3.61 deg forward**
Hinge Line	**-**	**54.34%**
Dihedral	**-**	**−4.00 deg**
Aspect Ratio	**-**	**2.93**
Mean Aerodynamic Chord	**-**	**1.147 m; 45.15 in.**

Fig. 5 T-38 damaged stabilator pressure and force wind-tunnel model [2].

along with the structural damage modeling, a new aeroelastic instability mechanism was theoretically identified, in addition to the well-known classical stiffness failure mechanisms of flutter and divergence. That is, the equations depicted in Fig. 10 represent the classical Mathieu–Hill equations that result from including an aerodynamic damage model in the problem formulation along with the traditional structural dynamics damage model. Because a time-dependent stiffness parameter has now been introduced into the equations of motion by the damage-induced unsteady aerodynamic modeling employing a drag term, a time-varying coefficient form of equations with a "parametric forcing function" has appeared, along with a classical right-hand-side forcing function in the equations of motion. The terms "parametric excitation" and "parametric response" are employed in this study following the traditions in nonlinear dynamics when a parameter of the system undergoes a changing value in time and introduces new possible response features that are more nonlinear in character [12]. In summary, parametrically excited limit cycle oscillations occurred when certain tuning or frequency selection rules were met between the excited fluid modes in the wake oscillations imposed by the aerodynamic damage and a structural normal mode or modes at air speed of the system. That is, parametric oscillatory motion could be observed well below the flow energy levels where classic flutter and divergence occurred. This form of instability was the theoretical finding of the phase 1 study, which also confirmed the existence of such parametric instabilities from wind-tunnel tests conducted on the F-111 model. This was illustrated in these earlier tests by employing higher-order spectra (HOS) signal processing techniques [13].

In general, due to both these theoretical and experimental phase 1 findings, the damage to a lifting surface was assumed to degrade the normal aircraft performance due to the possible generation of parametric aeroelastic responses of the aircraft lifting surfaces,

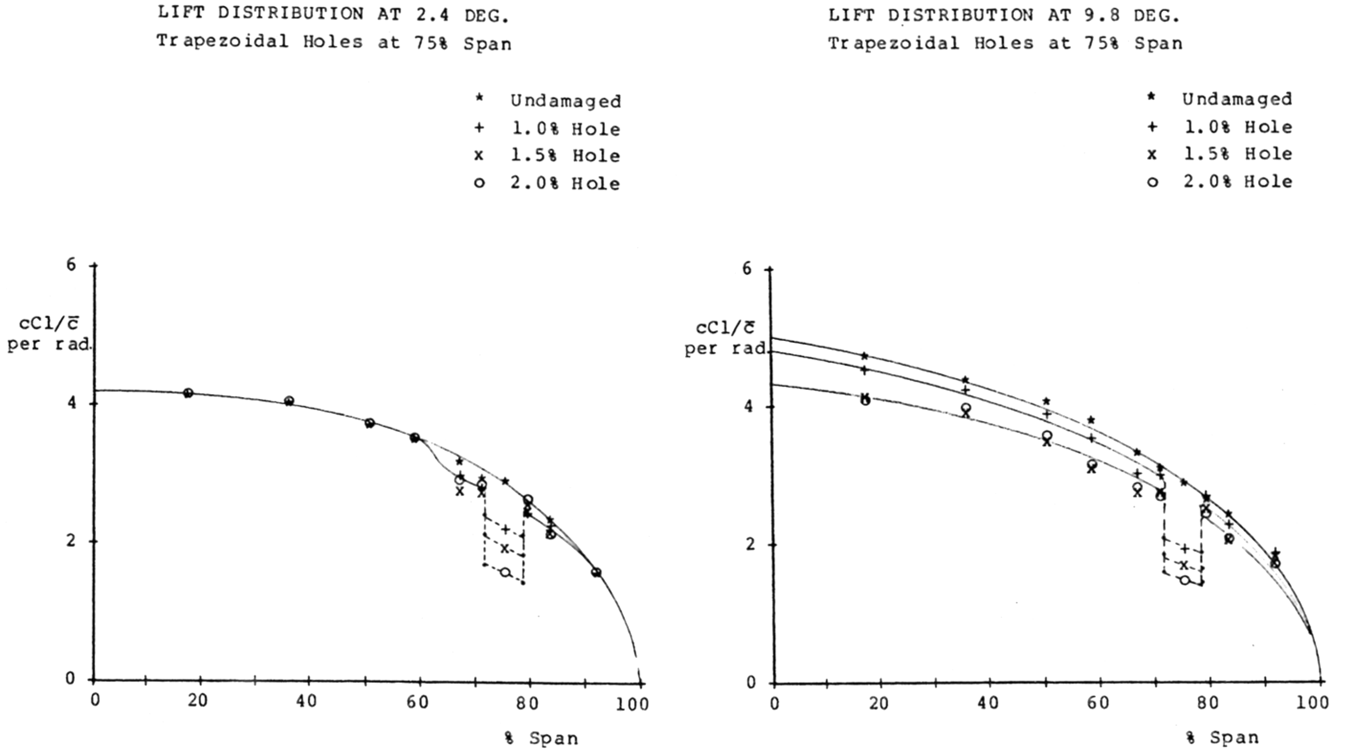

Fig. 6 Localization of aerodynamic damage spanwise load distributions at small angles of attack and propagation of perturbation loads at the higher angles of attack [1,2].

characterized by oscillations that are known as limit cycle oscillations. These LCOs exhibit a lock-in/lock-out mechanism depending on flow velocity. At the onset of this event, the random oscillations of the damaged-aircraft lifting surfaces due to airflow turbulence are subject to what appears to be a lock-in selection rule within a certain air-speed range to a parametric oscillation at a particular period of motion. When this occurs, the random oscillations become larger, occurring now at a specific frequency or period of motion with a more deterministic motion of response. As the air speed exceeds a certain range, however, the amplitude of the oscillation starts decreasing and returning to a more random motion as the parametric resonance or LCO stops responding. Although the energy levels of the LCOs are often too low to break the aircraft

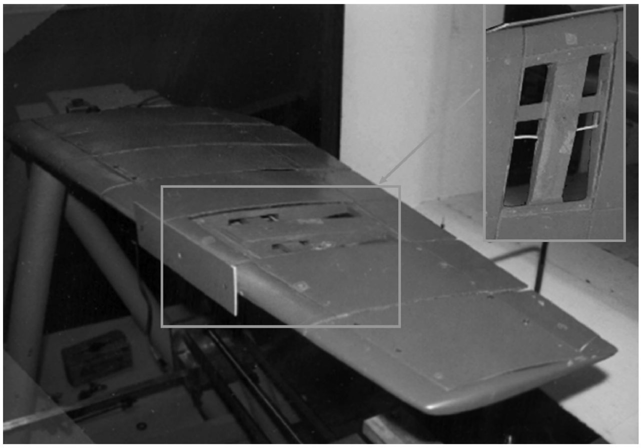

Fig. 7 Side view of the experimental setup for F-111 damaged wing (7 in. drag plate and through hole) [11].

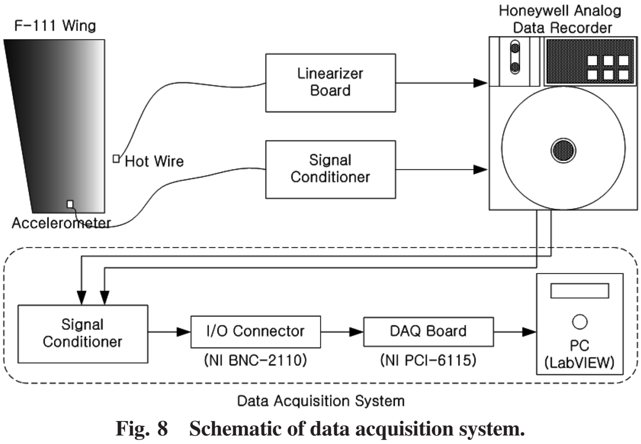

Fig. 8 Schematic of data acquisition system.

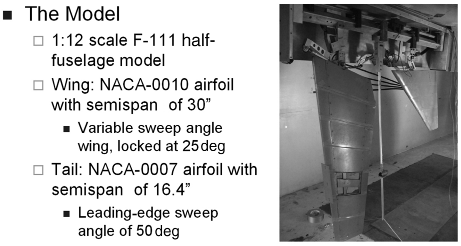

- The Model
  - ☐ 1:12 scale F-111 half-fuselage model
  - ☐ Wing: NACA-0010 airfoil with semispan of 30”
    - Variable sweep angle wing, locked at 25 deg
  - ☐ Tail: NACA-0007 airfoil with semispan of 16.4”
    - Leading-edge sweep angle of 50 deg

Fig. 9 Half-span F-111 (Wright–Patterson Flight Dynamics Laboratory design) wing-tail flutter model employed in damaged-wing study [34].

$$M\frac{d^2q}{dt^2}+C\frac{dq}{dt}+K(t)q=F(t)$$

$\Omega_f \approx 2\omega_n/k \quad \mathrm{k}=1,2,3....$ **: Parametric**

$\Omega_f \approx |\omega_i \pm \omega_j|/k \quad \mathrm{k}=1,2,3..... \text{and } (\mathrm{i} \neq \mathrm{j})$ **: Combination**

$|\Omega_{f1} \pm \Omega_{f2}| \approx \omega_n$ **: Mixed Mode**

Fig. 10 Aeroelastic in-flight warhead ballistic damage simulated by employing both a structural and aerodynamic model resulting in a classical Mathieu–Hill equations of motion allowing for limit cycle oscillation involving combination and parametric resonant instabilities [11].

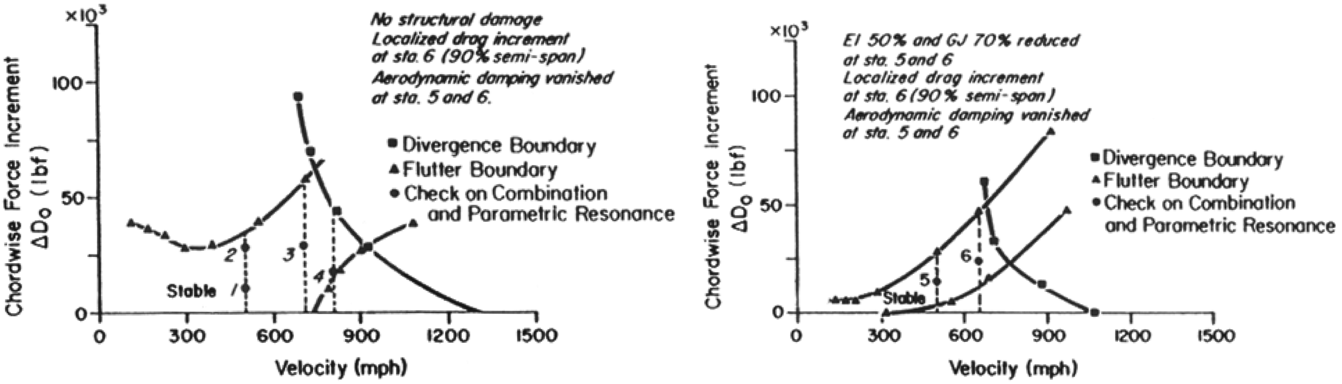

Flutter and divergence boundaries as influenced by aerodynamic damage model.

Flutter and divergence boundaries as influenced by both aerodynamic and structural damage models.

Fig. 11 Parametric and combination resonances embedded in the flutter and divergence free segment of the flight envelope [6].

structure, situations have occurred in which such oscillations have catastrophically upset the aircraft stability and control and/or have provided such an unacceptable ride quality as to inhibit good pilot operation of the aircraft [14].

V. Higher-Order Statistical Signal Processing

A. General Higher-Order Spectra Analysis

The lock-in/lock-out phenomenon appear to be nonlinear/parametric in nature. As the phenomenon occurs, "new" frequencies may be generated, caused by nonlinearities corresponding to harmonics and sum and difference combinations of the "original" frequencies. Not only do the original and new frequencies satisfy certain frequency selection rules, but they are also correlated by the introduction of a phase coupling, or phase coherence, between them. More specifically, the phase of each new frequency is related to the phase of the original primary interacting frequencies. Therefore, these phase couplings are a significant signature of true nonlinear interactions. Because the classical autopower spectrum contains no phase information, the phase coupling signature is not available. However, various higher-order spectra are capable of detecting such nonlinear-induced phase coupling [15]. Based on their advantages, HOS analysis techniques are used to analyze, interpret, and model the hot wire and accelerometer time series data described in Fig. 8.

1. Power Spectrum

Classical power spectra are one dimensional functions of frequency and have proven very powerful in modeling linear phenomena. For example, the discrete power spectrum is defined as

$$S_{XX}(k) = E\{X(k)X^*(k)\} \tag{1}$$

where $E\{\cdot\}$ denotes an expected value, k is discrete frequency, $X(k)$ denotes the discrete Fourier transform (DFT) of the stationary time series $x(n)$, and $*$ denotes the complex conjugate.

2. Bispectrum and Trispectrum

The next higher-order spectrum is the bispectrum, a two-dimensional function of frequency, which is very powerful in detecting and quantifying quadratic effects in a time series [16,17]. Let us assume that $x(n)$ is a zero-mean stationary random signal. The third-order moment spectrum, called the bispectrum, is defined as

$$S_{XXX}(i,j) = E\{X(i)X(j)X^*(k=i+j)\} \tag{2}$$

Note that the frequency selection rule $k = i + j$ should be satisfied, and k includes both sum and difference frequency interactions because the frequencies may be both positive and negative. Harmonic generation is a special case of $i = j$, and thus harmonics are included in bispectral analysis. For the bispectrum to be nonzero at (i, j), the Fourier transforms at i, j, and k must be nonzero. In addition, these three spectral components must be correlated; otherwise, when the expectation is carried out, the bispectrum will be zero due to random phase mixing. The correlation is usually provided by phase coupling associated with quadratic interactions. Unlike the power spectrum, even though $x(n)$ is a real valued time series, the bispectrum is complex. The value of the bispectrum at frequency coordinate (i, j) is determined by the degree of phase coupling between the Fourier components at i, j, and k. A very attractive feature of the bispectrum is that it is robust to additive Gaussian noise, because the bispectrum of additive Gaussian noise is ideally zero [18–21].

The spectrum of the fourth-order moment is called the trispectrum and can be defined as

$$S_{XXXX}(i,j,l) = E\{X(i)X(j)X(l)X^*(k=i+j+l)\} \tag{3}$$

The trispectrum is a three-dimensional function of frequency and can be interpreted as a natural extension of the bispectrum. Its advantages include the ability to detect and quantify cubic nonlinearities [17,22]. The frequency selection rule $k = i + j + l$ should be satisfied, and k includes both sum and difference frequency interactions because the frequencies may be both positive and negative. The value of the trispectrum at frequency coordinate (i, j, l) is determined by the degree of phase coupling between the Fourier components at i, j, l, and k.

3. Bicoherence and Tricoherence

The bispectrum and trispectrum given by Eqs. (2) and (3) may be used to identify the quadratic and cubic phase coupling signatures of lock in/lock out in an LCO, respectively. However, the bispectrum and trispectrum may suffer from one potential serious limitation, that is, the values are dependent not only on the degree of phase coupling but also on the amplitude of the interacting frequency components. This amplitude dependence makes it difficult to identify the degree of phase coupling, which is a true signature of nonlinearities in an LCO. To circumvent the amplitude dependence problem, one may use the bicoherence of Eq. (4) or tricoherence of Eq. (5) [23,24].

$$b^2(i,j) = \frac{|S_{XXX}(i,j)|^2}{E\{|X(i)X(j)|^2\}E\{|X(k=i+j)|^2\}} \tag{4}$$

The bicoherence of Eq. (4), which is essentially a normalized bispectrum, is independent of the amplitude of the Fourier transform, and the values of the squared bicoherence are bounded between zero and unity. Thus, the bicoherence is a useful measure of quadratic phase coupling introduced by quadratically nonlinear interactions or parametric interactions satisfying the frequency selection rule $k = i + j$. The normalized trispectrum is the tricoherence of Eq. (5).

$$t^2(i,j,l) = \frac{|S_{XXXX}(i,j,l)|^2}{E\{|X(i)X(j)X(l)|^2\}E\{|X(k=i+j+l)|^2\}} \tag{5}$$

The tricoherence is also independent of the amplitude of the Fourier transform, and the values of the tricoherence are bounded between zero and unity. As such, it quantifies the degree of cubic phase coupling between spectral components, satisfying the cubic frequency selection rule $k = i + j + l$.

The HOS concepts described in this section are applicable to only a single time series. However, in this paper, we are concerned with modeling the nonlinear relationship between the fluid flow (as provided by the hot-wire signal in Fig. 8) and the structural response (as provided by the accelerometer). To achieve this latter objective, we use a frequency-domain Volterra model described in next section.

B. Frequency-Domain Orthogonal Volterra Model Analysis

As indicated in previous section, even though the bicoherence and tricoherence enable us to define the presence of phase coupling when considering a single time series record [23,24], a more general approach is required when analyzing two or more time series records.

When two experimentally measured time series data can be interpreted as input and output, or excitation and response, the use of Volterra models has proven effective in modeling linear, quadratic, and cubic relationships between the two time series. Thus, to analyze the given damaged-wing model data and to search for nonlinear signatures of the lock-in/lock-out phenomenon from the hot wire and accelerometer time series data, we use a frequency-domain orthogonal third-order Volterra model to quantify the relationship between these two signals. The general discrete frequency-domain third-order Volterra model is given as

$$\hat{Y}(k) = H_L(k)X(k) + \sum_i \sum_j H_Q(i,j)X(i)X(j)\delta(k-i-j) + \sum_i \sum_j \sum_l H_C(i,j,l)X(i)X(j)X(l)\delta(k-i-j-l) \tag{6}$$

where i, j, k, and l are discrete frequencies, $X(k)$ is the DFT of the observed hot-wire excitation, $\hat{Y}(k)$ is the accelerometer response "predicted" by the model, δ denotes a Kronecker delta, and $H_L(k)$, $H_Q(i,j)$, and $H_C(i,j,l)$ denote the linear, quadratic, and cubic frequency-domain Volterra kernels or transfer functions, respectively. In addition, the block diagram of a general third-order Volterra model is illustrated in Fig. 12.

A key challenge is to determine the Volterra kernels from the DFTs of the hot-wire probe signal $X(k)$ and the accelerometer signal $Y(k)$ illustrated in Figure 8. The general approach is to estimate the Volterra kernels in such a way as to minimize the mean square error between the accelerometer response predicted by the model $\hat{Y}(k)$ and the true observed accelerometer response $Y(k)$. To do this, we need to characterize the statistics of the hot-wire signal using a hierarchy of higher-order spectra up to sixth order. Furthermore, we need to characterize the relation between the hot wire and accelerometer signals using a hierarchy of higher-order cross spectra up to fourth order. To develop a so-called orthogonal model, Gram–Schmidt techniques [25] are used. The details are beyond the scope of this paper, but further information is available [26–28].

The motivation for using Volterra model analysis arises from the fact that the frequency-domain Volterra model offers a number of advantages in modeling nonlinear physical phenomena. One of the advantages is the fact that once an appropriate Volterra model is obtained, it can be used to decompose an observed response into its constituent linear, quadratic, and cubic components as a function of frequency [29,30]. This property provides a conceptual framework within which to model the nonlinearities by extending the familiar concept of transfer function from linear to nonlinear systems.

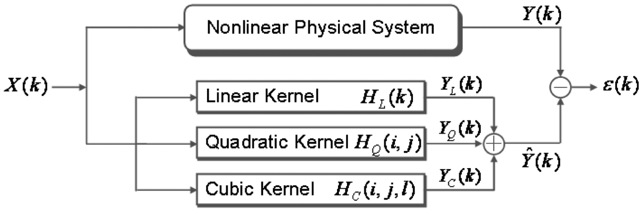

Fig. 12 Frequency-domain third-order Volterra model for system identification.

As indicated in Fig. 12, the output of general third-order Volterra model is as follows:

$$\hat{Y}(k) = Y_L(k) + Y_Q(k) + Y_C(k) \tag{7}$$

where $Y_L(k)$, $Y_Q(k)$, and $Y_C(k)$ are the outputs of the linear, quadratic, and cubic components of the Volterra model, respectively, as indicated in Fig. 12. Furthermore, $Y_L(k)$, $Y_Q(k)$, and $Y_C(k)$ correspond to the first, second, and third terms, respectively, on the RHS of Eq. (6).

The response power spectrum estimated by this model is given by

$$P_{\hat{Y}}(k) = E\{\hat{Y}(k)\hat{Y}^*(k)\} = E\{|Y_L(k)|^2\} + E\{|Y_Q(k)|^2\} + E\{|Y_C(k)|^2\} + 2\,\mathrm{Re}[E\{Y_L(k)Y_Q^*(k)\} + E\{Y_L(k)Y_C^*(k)\} + E\{Y_Q(k)Y_C^*(k)\}] \tag{8}$$

The last three terms are interference terms, which may be either positive or negative depending on the relative phases of $Y_L(k)$, $Y_Q(k)$, and $Y_C(k)$. The presence of such interference terms greatly hinders the interpretation of the Volterra model in terms of linear and nonlinear phenomena.

To alleviate the interference problem, orthogonalizing the Volterra model is indispensable [26–28]. Because we orthogonalize the Volterra model using the Gram–Schmidt procedure [25], the outputs of the linear, quadratic, cubic, etc., components of the Volterra model are orthogonal; thus, the interference terms are all zero. Therefore, the estimated power spectrum for our orthogonal model is

$$P_{\hat{Y}}(k) = E\{|Y_L(k)|^2\} + E\{|Y_Q(k)|^2\} + E\{|Y_C(k)|^2\} = P_L(k) + P_Q(k) + P_C(k) \tag{9}$$

We define the total model coherence $\gamma^2_{\mathrm{total}}(k)$ as the fraction of the true response power spectrum actually accounted for by the model

$$\gamma^2_{\mathrm{total}}(k) = \frac{P_{\hat{Y}}(k)}{P_Y(k)} \tag{10}$$

where the denominator is the true observed response power spectrum $P_Y(k) = E\{Y(k)Y(k)^*\}$, where $Y(k)$ is the DFT of the actual observed response in Fig. 12. The numerator is the power spectrum estimated by the model $P_{\hat{Y}}(k)$ at discrete frequency k indicated in Eq. (9).

Substituting Eq. (9) into Eq. (10) we get

$$\gamma^2_{\mathrm{total}}(k) = \frac{P_{\hat{Y}}(k)}{P_Y(k)} = \frac{P_L(k)}{P_Y(k)} + \frac{P_Q(k)}{P_Y(k)} + \frac{P_C(k)}{P_Y(k)} = \gamma_L^2(k) + \gamma_Q^2(k) + \gamma_C^2(k) \tag{11}$$

where $\gamma_L^2(k)$ is the linear coherence spectrum and represents the fraction of power observed in the output at frequency k that can be accounted for by the linear component of the model. Similarly, $\gamma_Q^2(k)$ is the quadratic coherence spectrum and represents the fraction of power observed in the output at frequency k that can be accounted for by the quadratic component, and $\gamma_C^2(k)$ is the cubic coherence spectrum and denotes the fraction of power observed in the output at frequency k that can be accounted for by the cubic component of the model. Thus, we can quantify the degree of linear, quadratic, and cubic contributions to the response of a nonlinear system at each frequency k. In this way, a quantitative indication is obtained of the relative contribution of linear, quadratic, and cubic phenomena to an experimentally observed response power spectrum. To investigate lock-in/lock-out phenomenon, we will plot $\gamma_L^2(k)$, $\gamma_Q^2(k)$, $\gamma_C^2(k)$, and $\gamma_{\text{total}}^2(k)$ vs airflow speed.

VI. Data Analysis and Results of the Study

A. Data Analysis

The damaged-wing wind-tunnel time series data was collected by Ortega [13] on analog magnetic tape. We played back the analog signals using an analog tape recorder, Honeywell 101 FM. We focused on two kinds of signals, namely the hot wire and accelerometer time series.

The airflow speed was measured through the hot-wire device positioned at the trailing edge of wing model and is considered as the observed excitation (i.e., input) $X(k)$ in Fig. 12. The oscillations of wing model are considered as system response (i.e., output) denoted by $Y(k)$ in Fig. 12 and were measured through the accelerometer placed on wing span.

The collection of the analog signals were digitized through our data acquisition system described earlier in Fig. 8. First, the analog signals were amplified by a signal conditioner. The amplified signals were then sampled by a data acquisition board through an I/O data acquisition connector. The data acquisition card was interfaced to a computer to process the sampled signals. LabVIEW was used to display and to store the sampled signals in binary format, and the stored data were further processed with our MATLAB®-based Volterra model to decompose the response power spectrum into its constituent linear, quadratic, and cubic components. That is, the four coherence spectra in Eq. (11) are calculated and plotted for various airflow speed settings.

A sampling rate of 1600 Hz was originally used during the digitizing procedure and each digitized signal was recorded for 5 min. Therefore, the total number of samples in each digitized data was 480,000 samples. Because the raw data showed little information above 200 Hz, the data was downsampled by a factor of 4 to yield an effective sampling rate of 400 Hz.

B. Experimental Results

Typical time series of the hot-wire sampling the flow just behind the wing aerodynamic damage area and the accelerometer sampling the vibration at the edge of the hole damaged wing are shown in the top and bottom traces of Fig. 13, respectively. The time interval is 2.5 s, and the mean flow speed is approximately 70.7 ft/s, which is a flow setting of approximately 7.5. The “air flow speed setting” is the index number imprinted on the wind-tunnel speed control knob used to control wind-tunnel speed settings. Table 1 gives the conversion from speed control number to the wind-tunnel flow velocity in ft/s indicated air speed. A parallel recording of the signals was carried out and recorded on a Honeywell model 101 analog tape recorder. Autopower spectra of the signals in Fig. 13 were estimated as shown in Fig. 14. The hot-wire autopower spectrum illustrates two spectral peaks at approximately 25 and 50 Hz, superimposed on a broader band of random noise extending to roughly 150–200 Hz. These spectral peaks represent the fluid normal modes resulting in normal-to-flow lift and rotational pitch moment forces occurring at 25 Hz, whereas the 50 Hz spectral peak represents the drag force parallel to the airstream. These fluid dynamic forces, due to the wake generated by the equivalent flat plate, interact with the structural normal modes to drive the wing into a periodic complex frequency limit cycle oscillation. The autopower spectrum of the accelerometer signal is shown in the bottom of Fig. 14 and demonstrates the excitation of the first several normal modes of the structure at this airflow speed. The frequency selection rules are illustrated in [11] and Fig. 10. A mixed mode of excitation, for example, illustrated in Fig. 10 occurs in Fig. 14 when the lift/moment forces at 25 Hz interact with the drag force at 50 Hz to excite a second torsion structural normal mode at 75 Hz. This was shown in [11] employing a cross-bicoherency HOS functional plot. Similar parametric interactions can be demonstrated between the normal modes of the fluid and the structure.

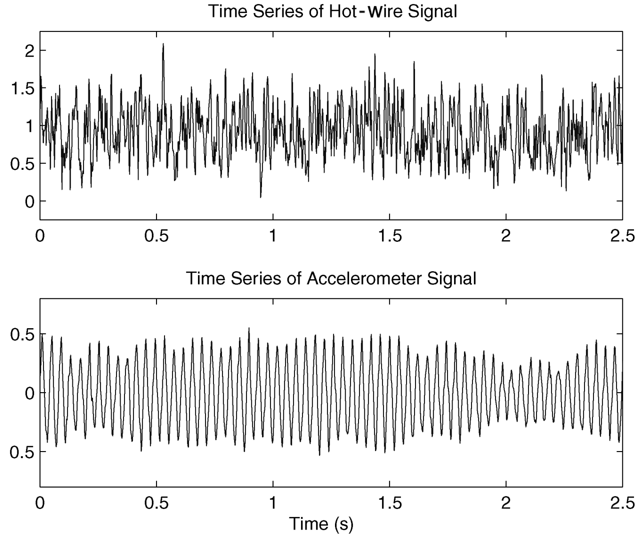

Fig. 13 Time series data of hot-wire device and accelerometer at lock in with airflow speed setting of 7.5.

Figure 15 illustrates how the power spectrum of the hot wire, and the accelerometer varies with airflow speed. The classical lift, moment, and drag forces identified by the hot wire in the Fig. 15a seem to occur as companion forces starting at the speed range of approximately 65 ft/s (airflow speed setting of about 7.0) (see Table 1). These fluid normal or spectral modes seem to be enhanced by the structural limit cycle response up to approximately 120 ft/s, which corresponds to an airflow speed setting of 12.0. Above this level, the drag spectrum diminished into a more random noise level at a speed setting of 13.0 or 14.0. Figure 15b shows an increase of accelerometer spectral response at a speed setting of approximately 6.0, or about 55 ft/s, where the two distinct hot-wire spectral peaks start to appear. The limit cycle response is thought to be well established in a zone up to about 12.0, where the higher spectral peaks above 130 Hz start diminishing. It is interesting that the lower spectral peaks around 25 Hz in both the hot-wire and the accelerometer signals stay dominant over the speed range.

Next we compute the frequency-domain orthogonal Volterra transfer functions $H_L(k)$, $H_Q(i,j)$, and $H_C(i,j,l)$ from the appropriate higher-order spectra. Then, all four terms $[P_{\hat{Y}}(k), P_L(k), P_Q(k), P_C(k)]$ in Eq. (9) are computed. After computing $P_Y(k)$ from the accelerometer signal, $\gamma_L^2(k)$, $\gamma_Q^2(k)$, $\gamma_C^2(k)$, and $\gamma_{\text{total}}^2(k)$ are computed via Eq. (11). This process is repeated for each airflow speed setting ranging from 2.0 to 13.0 (i.e., from 13.61 to 130 ft/s)

Table 1 Experimental values from wind-tunnel calibration [13]

Airflow speed setting	Air speed, ft/s
1.0	10.76
1.5	11.78
2.0	13.61
2.5	18.62
3.0	23.57
3.5	28.05
4.0	33.33
4.5	38.49
5.0	44.09
5.5	49.06
6.0	54.43
6.5	59.70
7.0	65.26
7.5	70.71
8.0	76.37
8.5	82.21
9.0	87.66
9.5	93.78
10.0	99.53
10.5	105.18
11.0	110.97

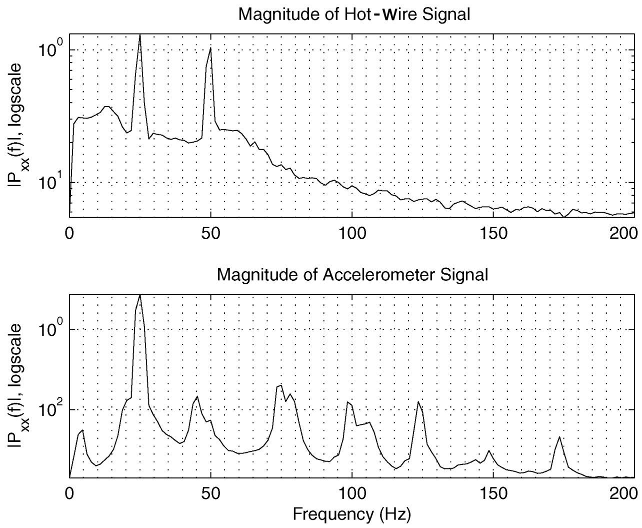

Fig. 14 Power spectra of hot-wire and accelerometer signals at lock in with airflow speed setting of 7.5.

[13]. The results are plotted in Fig. 16 as both 3-D and contour plots. The linear coherence $\gamma_L^2(k)$ in Fig. 16a is dominant at 25 and 50 Hz for airflow speed settings of 6.0–12.0, with a maximum occurring for air-speed settings of 7.0–9.0. The quadratic coherence $\gamma_Q^2(k)$ in Fig. 16b is dominant at 25, 75, and 100 Hz, and for airflow speed settings of 7.0–9.0. The cubic coherence spectrum $\gamma_C^2(k)$ in Fig. 16c indicates that cubic effects also tend to dominate at frequencies of 12, 25, and 125 Hz and for airflow speed settings of 7.0–9.0, although the values of $\gamma_C^2(k)$ are smaller than those of $\gamma_L^2(k)$ and $\gamma_Q^2(k)$. (Note that the peak values indicated on the color bars to the right of the contour plots are different for Figs. 16a–16d.) Finally, in Fig. 16d, we plot $\gamma_{\text{total}}^2(k) = \gamma_L^2(k) + \gamma_Q^2(k) + \gamma_C^2(k)$. These figures clearly show the dominant frequencies and the range of airflow speed settings of 7.0–9.0 at which quadratic and cubic effects appear to be important.

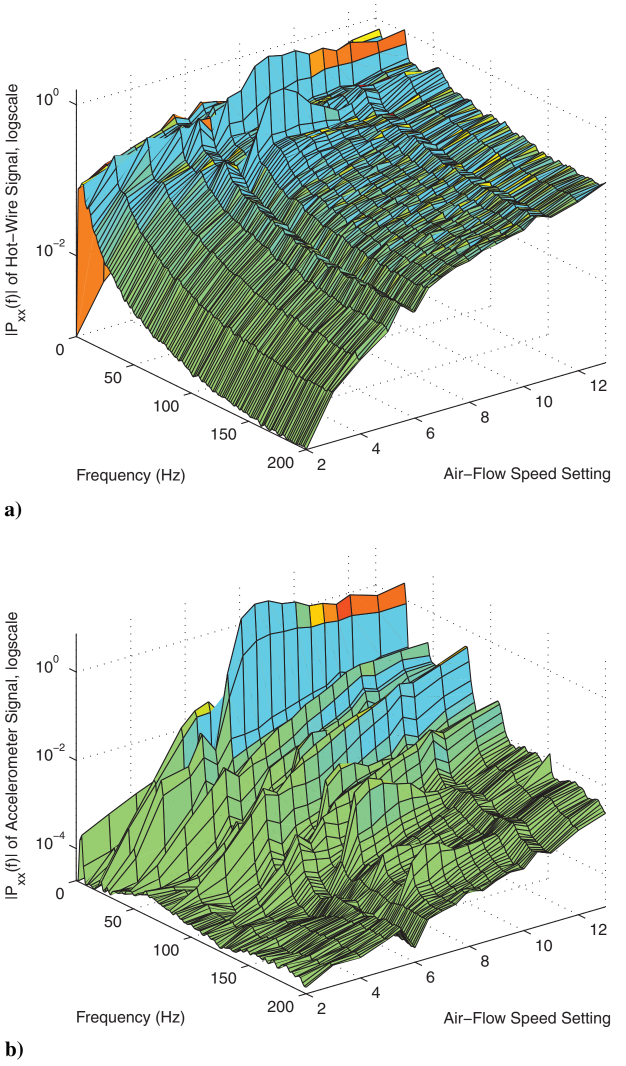

a)

b)

Fig. 15 Power spectra: a) hot-wire signal and b) accelerometer signal vs airflow speed settings.

The coherency comparison results in Fig. 16 suggest that a lock-in to lock-out limit cycle response occurs between 7.0–9.0 airflow speed setting range. This lock in/lock out of the damaged-wing LCO response feature is best illustrated in the quadratic and total coherency plots of Figs. 16b and 16d by the contour plots in the shape of islands at certain limited frequency and speed ranges. One of the more interesting and obvious observations of the data seen in the Figs. 16a–16d is that the linear and quadratic coherency levels dominate the total coherency response. The limit cycle parametric response is seen to be associated with mostly a quadratic nonlinear interaction. A closer look at our mathematical aeroelastic model presented in Fig. 10 does suggest that these derived parametric interactions evolving from our aerodynamic damage modeling give rise, for periodic time variations in the coefficients such as $K(t)$, to quadratic nonlinearities. The transformation of second-order dynamical equations of motion with periodic time varying coefficients can be made to a constant coefficient first-order Riccati (nonlinear) equation. This has been demonstrated in the classic book *Theory and Application of Mathieu Functions* [31].

The Riccati equation has quadratic nonlinearities only. This has also been stated in the classic text by Schetzen, who states a theorem that linear time varying systems can be identified by employing a second-order kernel from measured system inputs and outputs [32]. Bendat has mentioned this in one of his more recent text books [33]. In view of these mathematical observations, our experimental observations seem to be consistent with the solution forms of the proposed aeroelastic damage modeling.

VII. Conclusions

Earlier works on the damaged-wing aeroelastic modeling focused primarily on a structural dynamics wing damage model, which gave rise to a few anomalies. From about 1950 until around 1980, when our work with the Air Force first appeared, it became evident that some of the anomalies of these earlier studies could be cleared up if an aerodynamic damage model were also postulated. When this was carried out, after some extensive wind-tunnel testing on damage classes that generated high drag rise due to a jet wake spoiler effect, it became evident that a Mathieu–Hill system of equations seemed to better model these aeroelastic damage classes. This class of damage was found to give rise to torsionally dominant wing LCO responses on cantilever wing damage models investigated in the wind tunnel. That is, the presented experimental wind-tunnel studies further confirm the observations that the resulting nonlinear limit cycle modeling is best accomplished by means of a nonlinear quadratic form of equations as the result of physically including a higher-order unsteady periodic drag term caused by the jet wake damage effect. This is consistent with the observation that a Mathieu–Hill system of equations with periodic coefficients can be transformed to a constant coefficient Riccati equation with a periodic right-hand-side forcing function. That is, this Riccati equation possesses only a quadratic form of nonlinearity. The proposed aerodynamic damage modeling employed in this study assumed that a localized damage condition produces only a localized perturbation in the aerodynamic loads. However, wind-tunnel tests conducted by us over several years demonstrated that this was an approximation valid only over the smaller angles of attack, less than about 6 deg, in essence, only in the cruise range of the aircraft flight envelope. For the higher angles of attack encountered during maneuvering or possibly during some gust encounters, the localized damage effects were found to propagate significantly over the damaged surface in a manner similar to that

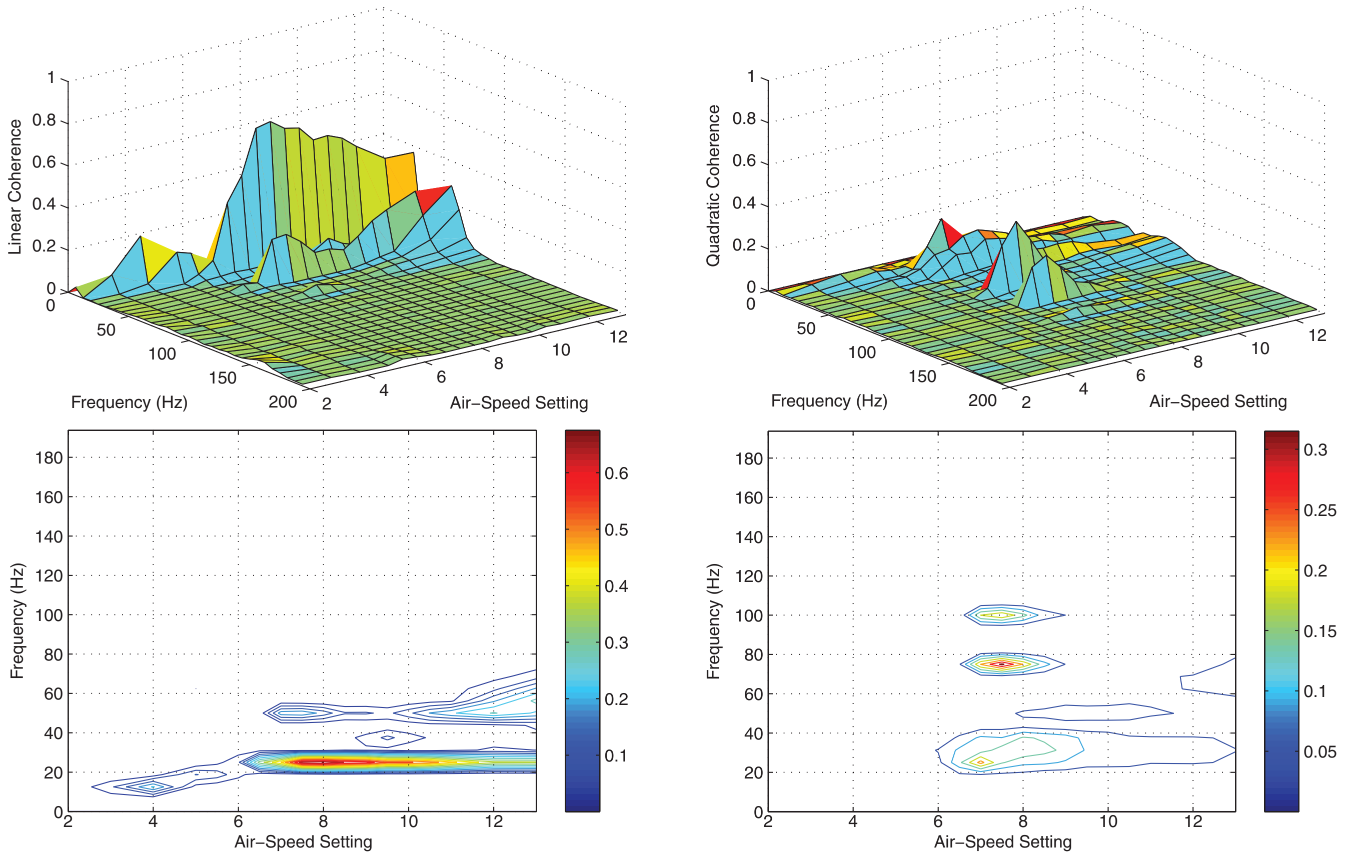

a)) Linear Coherence, $\gamma_L^2(k)$

b) Quadratic Coherence, $\gamma_Q^2(k)$

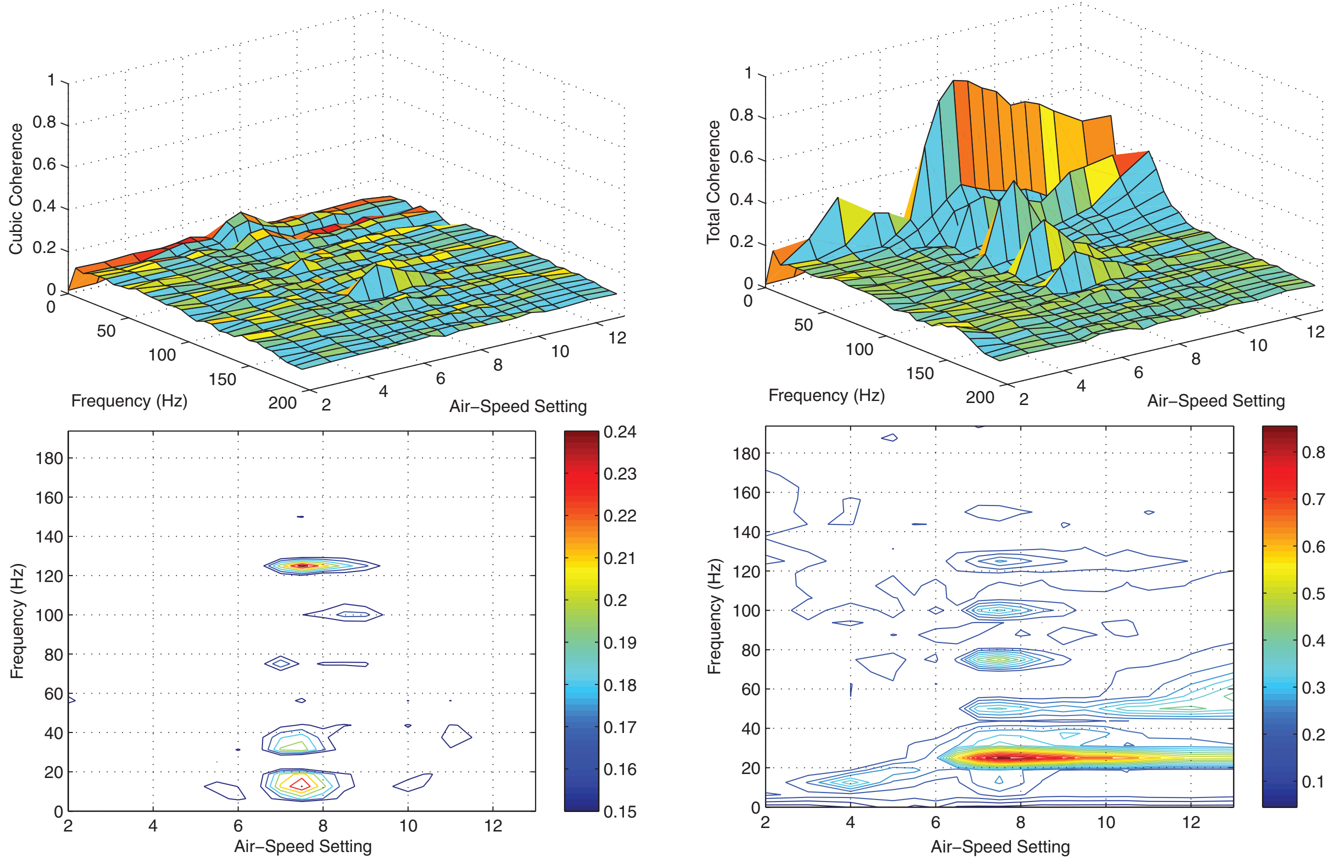

c) Cubic Coherence, $\gamma_C^2(k)$

d) Total Coherence, $\gamma_{total}^2(k)$

Fig. 16 Plots of a) $\gamma_L^2(k)$, b) $\gamma_Q^2(k)$, c) $\gamma_C^2(k)$, and d) $\gamma_{\mathrm{total}}^2(k)$ vs airflow speed settings. Note that the color bar scales are different in each figure.

found in a wing stall phenomenon. Finally, it was also experimentally observed that a similar LCO lock-in/lock-out phenomenon, first reported in the 1940 studies of the Tacoma Narrows Bridge failure investigations, also occurred in these wind-tunnel studies on the damaged wing.

Acknowledgment

We are grateful to E. G. Ortega, who collected the hot-wire and accelerometer time series data that were analyzed in this paper.

References

[1] Westkaemper, J. C., and Chandrsekharan, R. H., "The Effects of Warhead-Induced Damage on the Aeroelastic Characteristics of Lifting Surfaces, Vol II: Aerodynamic Effects," Air Force Office of Scientific Research TR-80-1039, July 1980.

[2] Westkaemper, J. C., and Chandrsekharan, R. H., "Effect on Surface Pressures of Trapezoidal Holes in a T-38 Stabilator," *Journal of Aircraft*, Vol. 19, No. 1, Jan. 1982, pp. 81–82. doi:10.2514/3.44746

[3] Broeren, A. P., Addy, H. E., and Bragg, M. B., "Flow Field Measurements About an Airfoil with Leading Edge Ice Shapes," AIAA Paper 2004-559, Jan. 2004.

[4] Peyus, A., "Refuges Flyways and Migratory WaterFowl," *FAA Aviation News*, Vol. 45, No. 5, Sept.–Oct. 2006, pp. 26–30.

[5] Allan, J. R., "The Cost of Bird Strikes and Bird Strike Prevention," *Proceedings of the Third NWRC Special Symposium*, Aug. 2000, pp. 147–153.

[6] Chen, G. S., and Stearman, R. O., "A Damage-Induced Failure Mode Involving Combination and Parametric Resonant Instabilities of Lifting Surfaces," AIAA Paper 1982-636, May 1982.

[7] Biot, M. A., and Arnold, L., "Study of Vulnerability of Aircraft to Damage Induced Flutter," Ballistic Research Laboratories, Rept. No. 743, 1950.

[8] Fung, Y. C., *An Introduction to the Theory of Aeroelasticity*, Dover, New York, 1969.

[9] Dowell, E. H., Curtiss, H. C. J., Scanlan, H., and Sisto, F., *A Modern Course in Aeroelasticity*, Sijhoff and Noordhoff, New York, 1978.

[10] Bragg, M. B., "Aerodynamics of Supercooled-Large-Droplet Ice Accretions and the Effect on Aircraft Control," *Proceedings of the FAA International Conference on Aircraft Inflight Icing*, Vol. 2, DOT/FAA/AR-96/81, Aug. 1996, pp. 387–399.

[11] Kruger, M. S., Endruhn, C. W., and Stearman, R. O., "A New Look at Galloping," AIAA Paper 2005-2178, April 2005.

[12] Panovko, Y. G., and Gubanova, I. I., *Stability and Oscillations of Elastic Systems: Paradoxes, Fallacies, and New Concepts*, Consultants Bureau Enterprises, Inc., New York, 1965.

[13] Ortega, E. G., "Utilization of Higher-Order Spectral Analysis to Characterize the Parametric and Nonlinear Aeroelastic Wing Responses Induced by Battle Damage," Master's Thesis, Department of Aerospace Engineering, University of Texas, Austin, TX, 1995.

[14] Stearman, R. O., Powers, E. J., Lee, Y. J., and Yukovich, R., "System Identification of Advanced Technology Aircraft Through Application of Higher Order Signal Processing," *2nd International Signal Processing Workshop in Higher Order Statistics*, July 1991.

[15] Boashash, B., Powers, E. J., and Zoubir, A. M. (eds.), *Higher-Order Statistical Signal Processing*, Longman–Wiley, Melbourne, New York, 1995.

[16] Kim, Y. C., and Powers, E. J., "Digital Bispectral Analysis and its Applications to Nonlinear Wave Interactions," *IEEE Transactions on Plasma Science*, Vol. PS-7, No. 2, 1979, pp. 120–131.

[17] Collis, W. B., White, P. R., and Hammond, J. K., "Higher-Order Spectra: The Bispectrum and Trispectrum," *Mechanical Systems and Signal Processing*, Vol. 12, No. 3, May 1998, pp. 375–394. doi:10.1006/mssp.1997.0145

[18] Arthur, N., and Penman, J., "Induction Machine Condition Monitoring with Higher Order Spectra," *IEEE Transactions on Industrial Electronics*, Vol. 47, No. 5, Oct. 2000, pp. 1031–1041. doi:10.1109/41.873211

[19] Chow, T. W. S., and Tan, H.-Z., "HOS-Based Nonparametric and Parametric Methodologies for Machine Fault Detection," *IEEE Transactions on Industrial Electronics*, Vol. 47, No. 5, Oct. 2000, pp. 1051–1059. doi:10.1109/41.873213

[20] Yang, D. M., Stronach, A. F., MacConnel, P., and Penman, J., "Third-Order Spectral Techniques for the Diagnosis of Motor Bearing Condition Using Artificial Neural Networks," *Mechanical Systems and Signal Processing*, Vol. 16, Nos. 2–3, 2002, pp. 391–411. doi:10.1006/mssp.2001.1469

[21] Mathews, V. J., and Sicuranza, G. L., *Polynomial Signal Processing*, Wiley, New York, 2000.

[22] Molle, J. W. D., and Hinich, M. J., "Trispectrum," *Proceedings of the Workshop Higher Order Spectral Analysis*, Vail, CO, 1989, pp. 68–72.

[23] Chabalko, C. C., Hajj, M. R., and Mook, D. T., "Characterization of the LCO Response Behavior of the NATA Model," AIAA Paper 2006-1852, May 2006.

[24] Hajj, M. R., and Beran, P. S., "Identification of Nonlinearities Responsible for Limit Cycle Oscillations of Fighter Aircraft," AIAA Paper 2007-1797, April 2007.

[25] Golub, G. H., and Loan, C. F. V., *Matrix Computations*, Dover, Baltimore, MD, 1989.

[26] Im, S., Kim, S. B., and Powers, E. J., "Orthogonal Development of a Discrete Frequency-Domain Third-Order Volterra Model," *Proceedings of the IEEE International Conference on Acoustics, Speech, and Signal Processing*, Vol. 4, April 1993, pp. 484–487.

[27] Im, S., and Powers, E. J., "A Sparse Third-Order Orthogonal Frequency-Domain Volterra-Like Model," *Journal of the Franklin Institute*, Vol. 333, No. 3, May 1996, pp. 385–412. doi:10.1016/0016-0032(96)00034-8

[28] Kim, S. B., and Powers, E. J., "Orthogonalized Frequency Domain Volterra Model for Non-Gaussian Inputs," *IEE Proceedings F, Radar Signal Processing*, Vol. 140, No. 6, Dec. 1993, pp. 402–409.

[29] Powers, E. J., Im, S., Kim, S. B., and Tseng, C. H., "Frequency-Domain Volterra Kernel Estimation via Higher-Order Statistical Signal Processing," *Asilomar Conference on Signals, Systems & Computers*, Vol. 16, Nov. 1993, pp. 446–450.

[30] Nam, S. W., and Powers, E. J., "Application of Higher-Order Spectral Analysis to Cubically Nonlinear System Identification," *IEEE Transactions on Signal Processing*, Vol. 42, No. 7, July 1994, pp. 1746–1765. doi:10.1109/78.298282

[31] McLachlan, N. W., *Theory and Application of Mathieu Functions*, Dover, New York, 1964.

[32] Schetzen, M., *The Volterra and Wiener Theories of Nonlinear Systems*, Wiley, New York, 1980.

[33] Bendat, J. S., *Nonlinear System Analysis and Identification from Random Data*, Wiley, New York, 1990.

[34] Park, H., Kim, T., Stearman, R., and Powers, E. J., "Wind Tunnel Studies of Damaged-Wing Induced Limit Cycle Oscillations," AIAA Paper 2007-1799, April 2007.